## Exchange magnetostriction in two-dimensional antiferromagnets

Shengwei Jiang<sup>1</sup>, Hongchao Xie<sup>1,2</sup>, Jie Shan<sup>1,3,4\*</sup>, Kin Fai Mak<sup>1,3,4\*</sup>

<sup>1</sup>Laboratory of Atomic and Solid State Physics, Cornell University, Ithaca, NY, USA.

<sup>2</sup>Department of Physics, Penn State University, University Park, Pennsylvania, USA

<sup>3</sup>School of Applied and Engineering Physics, Cornell University, Ithaca, NY, USA

<sup>4</sup>Kavli Institute at Cornell for Nanoscale Science, Ithaca, NY, USA

Email: iio shan@cornell.edu: kinfoi mak@cornell.edu

Email: jie.shan@cornell.edu; kinfai.mak@cornell.edu

These authors contributed equally: Shengwei Jiang, Hongchao Xie.

Magnetostriction, coupling between the mechanical and magnetic degrees of freedom, finds a variety of applications in magnetic actuation, transduction and sensing <sup>1,2</sup>. The discovery of two-dimensional (2D) layered magnetic materials <sup>3,4,5,6,7,8</sup> presents a new platform to explore the magnetostriction effects in ultrathin solids. Here we demonstrate an exchange-driven magnetostriction effect in mechanical resonators made of 2D antiferromagnetic CrI<sub>3</sub>. The mechanical resonance frequency is found to depend on the magnetic state of the material. We quantify the relative importance of the exchange and anisotropy magnetostriction by measuring the resonance frequency under a magnetic field parallel and perpendicular to the easy axis, respectively. Furthermore, we show efficient straintuning of the internal magnetic interactions in 2D CrI<sub>3</sub> as a result of inverse magnetostriction. Our results establish the basis for mechanical detection and control of magnetic states and magnetic phase transitions in 2D layered materials.

Two-dimensional (2D) layered magnetic materials are attractive systems for exploring magnetostrictive phenomena and applications: while they share high mechanical stiffness and strength and low mass with other 2D materials, they are magnetically active <sup>1,2,3,6,7,8</sup>. Among the large class of newly emerged 2D layered magnetic materials, of particular interest is few-layer CrI<sub>3</sub>, whose magnetic ground state consists of antiferromagnetically coupled ferromagnetic (FM) monolayers with out-of-plane easy axis <sup>3,5</sup>. The interlayer exchange interaction is relatively weak. A magnetic field on the order of 0.5 T in the out-of-plane ( $\hat{z}$ ) direction can induce a spin-flip transition in bilayer CrI<sub>3</sub>. Remarkable phenomena and device concepts based on detecting and controlling the interlayer magnetic state have been recently demonstrated, including spin-filter giant magnetoresistance <sup>9,10,11,12</sup>, magnetic switching by electric field <sup>13</sup> or electrostatic doping <sup>14,15,16,17</sup>, and spin transistors <sup>18</sup>. The coupling between the magnetic and mechanical degrees of freedom in the material, however, remains elusive.

Here we demonstrate exchange magnetostriction and its inverse effect in mechanical resonators made of 2D CrI<sub>3</sub> drumhead membranes (Fig. 1a). We focus on even-layer CrI<sub>3</sub> for maximum effect (see Supplementary Fig. S2 for an odd-layer case). We encapsulate

CrI<sub>3</sub> (an air sensitive insulator) within two stable 2D materials, few-layer graphene (below) and monolayer WSe<sub>2</sub> (above) (Fig. 1b). In addition to protect CrI<sub>3</sub> from degradation under ambient conditions, few-layer graphene acts as a conducting electrode, while monolayer WSe<sub>2</sub> as a strain gauge as we discuss below. The 2D heterostructure is first assembled and then transferred on prefabricated circular microtrenches (2 – 3  $\mu$ m in radius) with patterned Au electrodes and Si back gate. The optical image of a sample device is shown in Fig. 1c. We drive mechanical resonances in the membrane electrically in the linear regime using a small r.f. gate voltage (~ 1 mV). It is superposed on a DC gate voltage  $V_g$  that applies static tension to the membrane by pulling it towards the gate. We detect the mechanical resonances interferometrically at 633 nm using a network analyzer. We also measure the out-of-plane magnetization of the membrane using magnetic circular dichroism (MCD) at 633 nm. Unless otherwise specified, all measurements were performed at 4 K in a helium exchange gas environment (<10<sup>-5</sup> Torr). (See Methods for details on device fabrication and measurement techniques.)

Figure 1d shows the fundamental resonance mode of a bilayer  $CrI_3$  membrane at  $V_g = 0$ (the imperfect symmetry in the response to  $V_g > 0$  and  $V_g < 0$  gives rise to a net force at the r.f. driving frequency). It has a Lorentzian lineshape (solid line) with a peak frequency f around 25.5 MHz and a width around 10 kHz (corresponding to a quality factor of about 2500). Figure 1e shows the gate dependence of the resonance frequency. It is well described by the continuum model for a tensioned membrane with negligible bending stiffness and fully clamped boundary:  $f = \frac{\xi}{2\pi R} \sqrt{\frac{\sigma}{\rho}}$  (red solid line). Here  $\xi$  $\approx 2.405$  is the first root of the zeroth order Bessel function. The resonance frequency scales inversely with the drumhead radius R, and is determined by stress on the membrane  $\sigma$  and its 2D mass density  $\rho$ . Near  $V_g = 0$ , the resonance frequency is set by the built-in stress  $\sigma_0$ , whereas at higher  $V_g$  the gate-induced stress  $3Y_{eff} \epsilon(V_g)$  causes the frequency to increase roughly as  $V_q^4$ . Here  $Y_{eff}$  is the effective 2D Young's modulus of the membrane, and  $\epsilon(V_a)$  is the gate-induced strain. This behavior is fully consistent with other 2D mechanical resonators, including graphene and MoS<sub>2</sub> [Ref. <sup>19,20,21</sup>]. We calibrate  $\epsilon(V_a)$  from the exciton peak shift of the WSe<sub>2</sub> layer (63 meV per percent of biaxial strain <sup>22</sup>), and determine the parameters of the resonator  $\sigma_0 \approx 0.5$  N/m,  $Y_{eff} \approx 600$  N/m and  $\rho \approx 3 \times 10^{-5} \text{ kg/m}^2$  for the example shown in Fig. 1 [Ref. <sup>19,20,21</sup>] (see Methods).

 We investigate the effect of magnetic field on  $CrI_3$  resonators at  $V_g = 0$ . The mechanical resonance of the bilayer  $CrI_3$  device is measured while the field is swept from 1 T to -1 T back to 1 T along the easy axis  $\hat{z}$  (Fig. 2a). The resonance frequency f is independent of field except an abrupt redshift of  $\sim 0.06\%$  when the field magnitude exceeds  $\sim 0.5$  T. The linewidth and amplitude basically do not change (Supplementary Fig. S1). We correlate the field dependence of f (Fig. 2b) with MCD (Fig. 2c). MCD of the membrane is consistent with the reported results for bilayer  $CrI_3$  [Ref. <sup>14</sup>]. The material is antiferromagnetic (AF) under small fields (the finite MCD signal is caused by layer

asymmetry in the heterostructure) and undergoes a first-order AF-FM spin-flip transition (with hysteresis) around  $\pm 0.5$  T. The mechanical resonance frequency is thus correlated with the sample's magnetic state with  $f_{AF} > f_{FM}$ , where  $f_{AF}$  and  $f_{FM}$  denote the resonance frequency in the AF and FM state, respectively. In contrast to MCD, f is insensitive to the magnetization direction.

Similar behavior is observed in all CrI<sub>3</sub> resonators (6 in total) that were investigated in this study. Figure 2d - 2f shows the corresponding result for a 6-layer CrI<sub>3</sub> resonator under an out-of-plane field up to 2.3 T (see Supplementary Fig. S2 for the other devices). Compared to bilayer CrI<sub>3</sub>, there are now two spin-flip transitions around 0.9 T and 1.8 T, which correspond to spin flip in the surface layer and the interior layers, respectively  $^{9,18}$ . The resonance frequency redshifts at each spin-flip transition. The total redshift from  $f_{AF}$  ( $\sim 0$  T) to  $f_{FM}$  (>1.8 T) is about 0.23%. This is nearly 5 times larger than in bilayer CrI<sub>3</sub>.

The behavior of the resonators under an in-plane magnetic field is different. Figure 3a shows the mechanical resonance of the same 6-layer  $CrI_3$  device as in Fig. 2d - 2f while the magnetic field is swept from 8 T to -8 T to 8 T along the in-plane direction. The field dependence of f is shown in Fig. 3b after subtracting a small linear drift due to stress relaxation and/or slow temperature drift. Sharp transition and hysteresis that are characteristic of the first-order spin-flip transition are absent. Instead, f redshifts smoothly with increasing field and saturates beyond  $\sim$  6 T. The total change in f ( $\sim$  0.13%) is about half of the value observed under the out-of-plane field. Consistent behavior is observed in a second 6-layer device (Supplementary Fig. S3). The smooth redshift is correlated with the spin-canting effect observed in 2D  $CrI_3$  [Ref.  $^{9,18}$ ]. Because of the large out-of-plane magnetic anisotropy, the spins under an in-plane field are canted continuously from  $\hat{z}$  until reaching the saturation field, beyond which they are fully aligned with the field. The observed saturation field ( $\sim$  6 T) agrees with the value reported for multilayer  $CrI_3$   $^{23}$ . It is higher than in bilayer  $CrI_3$ , in consistence with the higher magnetic transition temperatures in thicker samples.

The resonance frequency of a mechanical resonator at  $V_g = 0$  is determined by the built-in stress  $\sigma_0$ . The observed correlation between the resonance frequency and the magnetic state of 2D CrI<sub>3</sub> suggests that magnetostriction is a result of competition between minimizing the elastic energy and the internal magnetic interactions. Other effects such as the one arisen from the magnetostatic energy cannot explain the experimental observations (see Methods). The elastic energy of a membrane per unit area can be expressed as  $U_{el} = \frac{3}{2} Y_{eff} \epsilon^2$  [Ref. <sup>19,20,21</sup>]. In our devices  $Y_{eff}$  is dominated by that of few-layer graphene and is independent of magnetic field (Methods); strain  $\epsilon = (a - a_0)/a_0$  is defined as a fractional change of the in-plane lattice constant a from its equilibrium value  $a_0$ . For fully clamped membranes with no vertical displacement, the boundary/substrate does work  $U_b = -\sigma_0 \epsilon = -2U_{el}$  to keep the area or in-plane lattice constant a of the membrane fixed. Here  $\sigma_0 = 3Y_{eff}\epsilon$  is the stress. If we neglect the strain

dependence of the demagnetization energy and leave out the intralayer exchange interactions (which do not play a role in the interlayer metamagnetic transition), the part of free energy that is strain dependent can be expressed to the lowest relevant order as

$$F = -J_{\perp}(\widehat{\mathbf{S}}_{t} \cdot \widehat{\mathbf{S}}_{b}) + K_{eff}(|\widehat{\mathbf{S}}_{t} \times \widehat{\mathbf{z}}|^{2} + |\widehat{\mathbf{S}}_{b} \times \widehat{\mathbf{z}}|^{2}), \tag{1}$$

for bilayer CrI<sub>3</sub>. Here  $\hat{S}_t$  and  $\hat{S}_b$  denote the spin unit vector of the top and bottom CrI<sub>3</sub> layers, respectively. The two terms describe, respectively, the interlayer exchange coupling with energy per unit area  $J_{\perp}$  (> 0 for FM and < 0 for AF ordering) and anisotropy with effective energy per unit area per layer  $K_{eff}$  (> 0). For simplicity we only consider the effect of bond length change on  $J_{\perp}$  and  $K_{eff}$ . The equilibrium lattice constant of the strained membrane in each magnetic state can be found by minimizing the total energy ( $U_{tot} = -U_{el} + F$ ) with respect to  $a_0$ , or equivalently strain  $\epsilon$ , from which stress and mechanical resonance frequency can be evaluated  $^{24}$  (see Methods).

For spin-flip transitions, the anisotropy energy is not relevant because spins are along the easy axis<sup>24,25,26</sup>. Minimizing  $U_{tot}$  for bilayer CrI<sub>3</sub> yields a change in strain  $(\frac{2}{3Y_{eff}}\frac{\partial J_{\perp}}{\partial \epsilon})$  and a fractional change in the resonance frequency  $(\frac{1}{3\sigma_0}\frac{\partial J_\perp}{\partial \epsilon})$  for the AF-FM transition. We estimate  $\frac{\partial J_{\perp}}{\partial \epsilon} A_u \approx +2$  meV from experiment, where  $A_u \ (\approx 0.41 \text{ nm}^2)$  is the unit cell area. The positive sign indicates that strain weakens AF ordering. We also estimate the saturation magnetostriction from the AF-FM transition induced strain change to be  $\sim 10^{-6}$ . It corresponds to intrinsic saturation magnetostriction of  $\sim 10^{-5}$  in bilayer CrI<sub>3</sub> because the Young's modulus of  $CrI_3$  is about an order of magnitude smaller than  $Y_{eff}$  of the heterostructure. The intrinsic value is comparable to that of elemental ferromagnetic metals <sup>27</sup>. The physical interpretation above is further supported by the nearly 5-time stronger magnetostrictive response in 6-layer CrI<sub>3</sub> than in bilayer CrI<sub>3</sub>. The interlayer exchange energy is 5 times larger in 6-layer CrI<sub>3</sub> since now there are 5 interfaces. 

energy. A similar energy minimization scheme can be applied to yield  $\frac{1}{3\sigma_0} \left(5 \frac{\partial J_\perp}{\partial \epsilon} - 6 \frac{\partial K_{eff}}{\partial \epsilon}\right) \left(\frac{H_\parallel}{H_S}\right)^2$  (for  $H_\parallel \leq H_S$ ) for the fractional resonance frequency shift in 6-layyer CrI<sub>3</sub>. Here  $H_\parallel$  and  $H_S$  are the applied and saturation field, respectively. The quadratic dependence of the resonance frequency shift on  $H_\parallel$  is in good agreement with experiment (dashed line, Fig. 3b). The discrepancy at small fields likely reflects a non-perfect alignment of the field with the sample plane. The observed  $\sim 50\%$  smaller frequency shift under saturation in Fig. 3b compared to Fig. 2e suggests that  $\frac{\partial K_{eff}}{\partial \epsilon} \approx \frac{1}{2} \frac{\partial J_\perp}{\partial \epsilon}$  in the 6-layer CrI<sub>3</sub> device. The stronger dependence on in-plane strain of the interlayer exchange than

Under an in-plane field, both interlayer exchange and anisotropy contribute to the free

the intralayer anisotropy is somewhat counterintuitive. Future studies are required to better understand this observation.

Finally, we use the mechanical device platform to demonstrate strain-tuning of the magnetic interactions through the inverse magnetostriction effect. We probe the spin-flip transition in the same bilayer  $CrI_3$  device as in Fig. 2a-c at different  $V_g$ 's by MCD (see Supplementary Fig. S4 for the study on a 6-layer device). The application of  $V_g$  can induce tension on the suspended membrane by an electrostatic force. It can also induce electrostatic doping into CrI<sub>3</sub> through the graphene layer because of its large quantum capacitance from the flat 3d bands 14,15. Figure 4a and 4b compare the behavior of a suspended and substrate-supported region of the membrane. Only the MCD data near the spin-flip transition for the positive field sweeping direction is shown for clarity. For the substrate-supported region, only the electrostatic doping effect is relevant. The spin-flip transition field  $H_C$  varies linearly with  $V_g$  (red symbols, Fig. 4c), which is in good agreement with previous studies <sup>14,15</sup>. In contrast, the behavior of the suspended region is almost symmetric about  $V_g = 0$ ;  $H_C$  decreases nonlinearly with  $V_g$  (blue symbols, Fig. 4c). We conclude from the comparison that electrostatic doping into suspended CrI<sub>3</sub> is not significant because of the low gate dielectric constant (vacuum) and the change in  $H_C$  is caused primarily by strain.

Figure 4d shows  $H_C$  as a function of gate-induced strain calibrated by the WSe<sub>2</sub> gauge. It decreases linearly with strain by as much as 32 mT. Quantitatively,  $H_C$  can be related to the interlayer exchange coupling  $J_{\perp}$  through  $\mu_0 H_C = \frac{-J_{\perp} + \mu_0 M_0^2/t}{M_0}$  [Ref. <sup>14</sup>], where  $\mu_0$ ,  $M_0$  and t denote the vacuum permeability, the saturation magnetization per CrI<sub>3</sub> monolayer, and the interlayer distance in bilayer CrI<sub>3</sub>, respectively (see Methods). We obtain  $\frac{\partial J_{\perp}}{\partial \epsilon} A_u \approx +4$  meV from the slope in Fig. 4d and  $M_0$  (assuming that each Cr<sup>3+</sup> cation carries a magnetic moment of 3 Bohr magnetons). The value agrees well with that estimated from the mechanical resonance measurement. The discrepancy is largely due to uncertainty in the resonator parameters (such as initial stress and mass). Nevertheless, the good agreement between two independent measurements illustrates the importance of interlayer exchange magnetostriction in 2D CrI<sub>3</sub>.

In conclusion, we have demonstrated an exchange magnetostriction effect in 2D antiferromagnetic CrI<sub>3</sub>. An inverse magnetostriction effect has also been demonstrated, which allows continuous strain-tuning of the internal magnetic interactions. Our results have put in place the groundwork for potential applications of these devices, including magnetic actuation and sensing, and for mechanical detection of emerging magnetic states and phase transitions in 2D layered magnetic materials <sup>28</sup>.

Methods

**Device fabrication** 

We used the layer-by-layer dry transfer method to fabricate drumhead resonators made of atomically thin CrI<sub>3</sub> fully encapsulated by few-layer graphene and single-layer WSe<sub>2</sub> as shown in Fig. 1b. Atomically thin flakes of CrI<sub>3</sub>, graphene and WSe<sub>2</sub> were mechanically exfoliated onto silicon substrates with a 285-nm oxide layer from the corresponding bulk synthetic crystals (from HQ Graphene). A polymer stamp made of a thin layer of polycarbonate (PC) on polydimethylsiloxane (PDMS) was used to pick up the desired flakes to form the heterostructure. The complete heterostructure was first released onto a new PDMS substrate so that the residual PC film on the sample can be removed by dissolving it in N-Methyl-2-pyrrolidone. The sample was then transferred onto a circular microtrench of  $2-3 \mu m$  in radius and 600 nm in depth on a silicon substrate with prepatterned Ti/Au electrodes. A small amount of PDMS residual was left untreated. Samples of CrI<sub>3</sub> were handled inside a nitrogen-filled glovebox with oxygen and water less than 1 part per million (ppm) to avoid degradation. The thickness of atomically thin materials was first estimated by their optical reflection contrast and then measured by atomic force microscopy (AFM). The thickness of WSe<sub>2</sub> flakes was verified by optical reflection spectroscopy. The thickness of CrI<sub>3</sub> flakes was further verified by the magnetization versus out-of-plane magnetic field measurement. Six devices (two bilayers, one trilayer and three 6-layers) were studied. Devices with 4-layer and 5-layer CrI<sub>3</sub> samples were not investigated. Their behaviors are expected to be similar to the ones covered in this study.

#### **Mechanical resonance detection**

219220

221

222

223224

225

226

227

228

229

230231

232

233

234

235

236

237238

239

240

241

242

243

244

245

246

247

248

249

250251

252253

254

255

256

257

258259

260

An optical interferometric technique was applied to detect the out-of-plane displacement of the resonators <sup>19,21,29</sup> (Fig. 1a). The resonators were mounted in a closed-cycle cryostat (Attocube, attoDry1000). The output of a HeNe laser at 632.8 nm was focused onto the center of the suspended membrane using a high numerical aperture (N.A. = 0.8) objective. The beam size on the device was on the order of 1  $\mu$ m and the total power was kept below 1  $\mu$ W to minimize the laser heating effect. The reflected beam was collected by the same objective and detected by a fast photodetector. Motion of the membrane was actuated capacitively by applying a small r.f. voltage (~ 1 mV) between the membrane and the back gate. As the membrane moves in the out-of-plane direction, the optical cavity formed between the membrane and the trenched substrate modulates the reflectance. The amplitude of the motion as a function of driving frequency was measured by a network analyzer (Agilent E5061A), which provided the r.f. voltage and measured the fast photodetector response. The amplitude of the motion reaches its maximum when the driving frequency matches the natural frequency of the resonator. The signal-to-noise ratio (SNR) for typical measurements is around 100. It gives rise to a strain detection sensitivity of  $\delta \epsilon \approx \frac{2}{Q \cdot SNR} \epsilon \sim 10^{-8}$ , where the mechanical quality factor Q is  $\sim 2000$  and the initial strain  $\epsilon$  is  $\sim 10^{-3}$ . This value is comparable to the performance of high-strain-sensitivity magneto-strain sensors <sup>30</sup>.

### Magnetic circular dichroism (MCD) measurements

MCD was employed to characterize the membranes' magnetic properties. A nearly identical optical setup as the one used for the mechanical resonance detection was employed. The polarization of the optical excitation at 632.8 nm was modulated between left and right circular polarization by a photoelastic modulator at 50.1 kHz. Both the AC and DC components of the reflected beam were detected by a photodiode in combination with a lock-in amplifier and multimeter, respectively. MCD was determined as the ratio of the AC to DC component.

# Strain calibration

261 262

263

264 265

266

267 268

269

270

271 272

273

274

275

276

277

278

279

280 281

282 283

284

It is challenging to determine the gate-induced strain  $\epsilon(V_a)$  in the suspended membranes from the gate dependence of the resonance frequency (Fig. 1e) using the continuum model described in the text. Many parameters of the resonator are involved and cannot be determined independently. Instead, we determine  $\epsilon(V_q)$  by using monolayer WSe<sub>2</sub> as a strain gauge assuming no relative sliding between WSe<sub>2</sub> and CrI<sub>3</sub> layers. It relies on the fact that the fundamental exciton resonance energy in monolayer WSe<sub>2</sub> redshifts linearly with strain (63 meV/%) for a relatively large rage of biaxial strain <sup>22</sup>. The fundamental exciton energy in monolayer  $WSe_2$  was determined as a function of  $V_g$  by optical reflection spectroscopy. In this measurement, broadband radiation from a single-mode fiber-coupled halogen lamp was employed as the source. A spectrometer equipped with a charge-coupled-device (CCD) camera was used for detection. The excitation power on the device was kept well below 0.1  $\mu$ W to minimize the laser heating effect. The gate dependence of the exciton resonance energy and the calibrated gate-induced strain is shown in Supplementary Fig. S5.

# Characterization of resonator parameters

285 By minimizing the sum of the elastic energy and the electrostatic energy with respect to 286 strain (i.e.  $\frac{\partial}{\partial \epsilon} \left[ \frac{3}{2} Y_{eff} \epsilon^2 - \frac{1}{2} C_g V_g^2 \right] = 0$ ), we obtain the gate-induced strain  $\epsilon (V_g) \approx$ 287  $\frac{1}{96} \left(\frac{R}{D}\right)^2 \left(\frac{\varepsilon_0 V_g^2}{D\sigma_0}\right)^2 \propto V_g^4$  for  $\epsilon(V_g) \ll \epsilon_0$  (the built-in strain). Here the back gate capacitance 288  $C_a$  is strain or gate dependent because of the gate-induced vertical displacement z of the 289 membrane, D is the vertical separation between the membrane and the back gate at  $V_g = 0$ , 290 R is the drumhead radius, and  $\varepsilon_0$  is the vacuum permittivity. The built-in stress  $\sigma_0$  can be 291 obtained from the slope of  $\epsilon(V_g)$  as a function of  $V_g^4$  (Supplementary Fig. S5c). The 292 effective Young's modulus  $Y_{eff}$  and the 2D mass density  $\rho$  of the membrane can be 293 obtained by fitting the experimental gate dependence of the resonance frequency using 294  $f = \frac{\xi}{2\pi R} \sqrt{\frac{\sigma}{\rho}}$  with  $\sigma = \frac{R^2}{4} \frac{\partial^2}{\partial z^2} \left[ \frac{3}{2} Y_{eff} \epsilon^2 - \frac{1}{2} C_g V_g^2 \right]$  [Ref. 19,20,21]. The extracted values for 295 bilayer CrI<sub>3</sub> resonator 1 are  $\sigma_0 \approx 0.5~Nm^{-1}$ ,  $\rho \approx 3 \times 10^{-5}~kgm^{-2}$ , and  $Y_{eff} \approx 600$ 296  $Nm^{-1}$ . The mass density is 1.9 times of the expected mass density of the heterostructure 297 presumably due to the presence of polymer residues and other adsorbates on the 298 299 membrane. The effective Young's modulus is also consistent with the expected value. We estimate the effective Young's modulus of 2D heterostructures as the total 300 contribution of constitute layers,  $Y_{eff} = \sum_{i} n_i Y_{2D,i}$ , where  $n_i$  and  $Y_{2D,i}$  are the layer 301 number and the 2D elastic stiffness per layer of the i-th material. We obtain  $Y_{eff} \approx$ 302

 $1200 \ Nm^{-1}$  for bilayer device 1 using the reported value for  $Y_{2D,g}=340 \ Nm^{-1}, Y_{2D,CrI_3}=25 \ Nm^{-1}$  and  $Y_{2D,WSe_2}=112 \ Nm^{-1}$  [Ref.  $^{31,32,33,34}$ ]. The Young's modulus is dominated by the contribution of graphene in most devices studied in this work, which typically consist of 3 layers of graphene, monolayer WSe<sub>2</sub>, and 2-6 layers of CrI<sub>3</sub>.

303 304 305

306 307

308

309 310

311

312

313

314

315

316

317

318

# Mechanisms for mechanical resonance shift in 2D CrI<sub>3</sub> under a magnetic field

In the main text, we have assigned the competition between the internal magnetic interactions and elastic energy as the major mechanism for the observed mechanical resonance shift in 2D CrI<sub>3</sub> resonators under a magnetic field at  $V_g = 0$ . Other effects could potentially also give rise to a mechanical resonance shift in 2D CrI<sub>3</sub>. One such possibility is the magnetostatic pressure from the gradient of the magnetostatic energy in the  $\hat{z}$ direction,  $\mathbf{M} \cdot \frac{\partial \mathbf{B}}{\partial \tau}$ . Here  $\mathbf{M}$  is the sample magnetization and  $\mathbf{B}$  is the magnetic field at the sample. However, for a nanometer thick sample with a lateral size of a few microns the gradient is expected to be negligible. This is supported by the absence of field dependence for the mechanical resonance up to high fields except at the spin-flip transitions (Supplementary Fig. S6).

319 320 321

322

323

#### Model for exchange magnetostriction in bilayer CrI<sub>3</sub>

We consider bilayer CrI<sub>3</sub> under an out-of-plane magnetic field  $\mu_0 H_1$ . The free energy per unit area for a free membrane in the AF and FM state in the zero-temperature limit can be expressed as

324 325 326

$$F_{AF} = 2F_0 + J_1, (S1)$$

$$F_{AF} = 2F_0 + J_{\perp}, \tag{S1}$$
 
$$F_{FM} = 2F_0 - J_{\perp} - 2\mu_0 M_0 \left( H_{\perp} - \frac{M_0}{t} \right). \tag{S2}$$

328 329

330 331

332

333

334

335

336

337

338

327

Here  $F_0$ ,  $M_0$ ,  $J_{\perp}$  and t denote the free energy of each monolayer, saturation magnetization of each layer, interlayer exchange interaction, and interlayer distance, respectively. The spin-flip field  $\mu_0 H_C$  can be evaluated by requiring  $F_{AF} = F_{FM}$  [Ref. <sup>13</sup>]. In the presence of fixed boundary, strain is developed with an elastic energy of  $U_{el} = \frac{3}{2} Y_{eff} \epsilon^2$ , where  $\epsilon = (a - a_0)/a_0$  is the fractional change of the in-plane lattice constant a (which is fixed by the boundary) from its equilibrium value  $a_0$ . To determined the equilibrium lattice constants  $a_{AF}$  and  $a_{FM}$  for the two states at the spin-flip transition, we consider the total energy  $U_{tot} = U_{el} + F + U_b$ . The last term  $U_b = -\sigma_0 \epsilon = -2U_{el}$  takes into account the work done by the boundary/substrate to keep the area of the membrane fixed, i.e in-plane lattice constant a fixed. By taking the derivative of the total energy with respect to strain, we obtain

339 340 341

$$\frac{\partial (-U_{el} + F_{AF})}{\partial \epsilon} = 2 \frac{\partial F_0}{\partial \epsilon} + \frac{\partial J_{\perp}}{\partial \epsilon} - 3Y_{eff} \epsilon_{AF} = 0 , \qquad (S3)$$

342 343

$$\frac{\partial (-U_{el} + F_{FM})}{\partial \epsilon} = 2 \frac{\partial F_0}{\partial \epsilon} - \frac{\partial J_\perp}{\partial \epsilon} - 3Y_{eff} \epsilon_{FM} = 0.$$
 (S4)

344 345

346

The strain dependence of  $M_0$  is ignored. The change of strain in the AF and FM states  $\epsilon_{AF}$  and  $\epsilon_{FM}$  can be found by subtracting (S3) from (S4)

347
$$\epsilon_{AF} - \epsilon_{FM} = \frac{2}{3Y_{eff}} \frac{\partial J_{\perp}}{\partial \epsilon}.$$
(S5)

350 The fractional change in the resonance frequency can be expressed as

 $\frac{f_{AF} - f_{FM}}{f_{AF}} \approx \frac{\sigma_{AF} - \sigma_{FM}}{2\sigma_{AF}} = \frac{1}{3\sigma_0} \frac{\partial J_{\perp}}{\partial \epsilon},$  (S6)

since  $f \propto \sqrt{\sigma}$ . Here we have taken the initial state to be AF. From experiment, we obtain  $\frac{\partial J_{\perp}}{\partial \epsilon} > 0$ , which corresponds to  $\epsilon_{AF} - \epsilon_{FM} > 0$  according to Eq. (S5). The lattice constant of CrI<sub>3</sub> in the AF state is smaller than in the FM state.

For in-plane magnetic fields, minimizing  $U_{tot}$  with respect to strain [with F given by Eqn. (1)] yields

361 
$$\frac{f_{AF} - f_{FM}}{f_{AF}} \approx \frac{1}{3\sigma_0} \left( \frac{\partial J_{\perp}}{\partial \epsilon} - 2 \frac{\partial K_{eff}}{\partial \epsilon} \right) \sin^2 \theta. \tag{S7}$$

Here  $\theta$  is the spin canting angle, which is related to the applied and saturation magnetic fields as  $\sin \theta = \frac{H_{\parallel}}{H_S}$  for  $H_{\parallel} \leq H_S$ . The result can be generalized to 6-layer CrI<sub>3</sub> as presented in the main text.

### References

349

351

357

358 359

360

362

363

364

365 366 367

368

<sup>&</sup>lt;sup>1</sup> Joule, J. P. On the effects of magnetism upon the dimensions of iron and steel bars. *Philos. Mag.* **30**, 76–87 (1847).

<sup>&</sup>lt;sup>2</sup> du Trémolet de Lacheisserie, E. Magnetostriction: Theory and Application of Magnetoelasticity. CRC Press, Boca Raton, 1993.

<sup>&</sup>lt;sup>3</sup> Mak, K. F., Shan, J. & Ralph, D. C. Probing and controlling magnetic states in 2D layered magnetic materials. *Nat. Rev. Phys.* **1**, 646–661 (2019).

<sup>&</sup>lt;sup>4</sup> Gong, C. et al. Discovery of intrinsic ferromagnetism in two-dimensional van der Waals crystals. Nature **546**, 265–269 (2017).

<sup>&</sup>lt;sup>5</sup> Huang, B. et al. Layer-dependent ferromagnetism in a van der Waals crystal down to the monolayer limit. Nature **546**, 270–273 (2017).

<sup>&</sup>lt;sup>6</sup> Gong, C. & Zhang, X. Two-dimensional magnetic crystals and emergent heterostructure devices. Science. **363**, eaav4450 (2019).

<sup>&</sup>lt;sup>7</sup> Gibertini, M., Koperski, M., Morpurgo, A. F. & Novoselov, K. S. Magnetic 2D materials and heterostructures. *Nat. Nanotechnol.* **14**, 408–419 (2019).

<sup>&</sup>lt;sup>8</sup> Burch, K. S., Mandrus, D. & Park, J.-G. Magnetism in two-dimensional van der Waals materials. *Nature* **563**, 47–52 (2018).

<sup>&</sup>lt;sup>9</sup> Song, T. et al., Giant tunneling magnetoresistance in spin-filter van der Waals heterostructures. Science **360**, 1214–1218 (2018)

<sup>10</sup> Klein, D. R. et al., Probing magnetism in 2D van der Waals crystalline insulators via electron tunneling. Science **360**, 1218–1222 (2018)

<sup>11</sup> Kim, H. H. et al., One million percent tunnel magnetoresistance in a magnetic van der Waals heterostructure. Nano Lett. 18, 4885–4890 (2018)

Wang, Z. et al., Very large tunneling magnetoresistance in layered magnetic semiconductor CrI3. Nat. Commun. 9, 2516 (2018)

<sup>13</sup> Jiang, S., Shan, J., Mak, K. F., Electric-field switching of two-dimensional van der Waals magnets. Nat. Mater. 17, 406–410 (2018)

<sup>14</sup> Jiang, S., Li, L., Wang, Z., Mak, K. F. & Shan, J. Controlling magnetism in 2D CrI<sub>3</sub> by electrostatic doping. Nat. Nanotechnol. 13, 549–553 (2018).

<sup>15</sup> Huang, B. et al. Electrical control of 2D magnetism in bilayer CrI<sub>3</sub>. Nat. Nanotechnol. **13**, 544–548 (2018)

<sup>16</sup> Jin, C. et al. Imaging and control of critical spin fluctuations in two-dimensional magnets, arXiv:1910.13023.

<sup>17</sup> Wang, Z. et al. Electric-field control of magnetism in a few-layered van der Waals ferromagnetic semiconductor. Nat. Nanotechnol. 13, 554–559 (2018).

<sup>18</sup> Jiang, S., Li, L., Wang, Z., Mak, K. F. & Shan, J. Spin transistor built on 2D van der Waals heterostructures. Nat. Electron. 2, 159–163 (2019).

<sup>19</sup> Bunch, J. S. et al. Electromechanical Resonators from Graphene Sheets. Science 315, 490-493 (2007).

<sup>20</sup> Chen, C. et al. Performance of monolayer graphene nanomechanical resonators with electrical readout. Nat. Nanotechnol. 4, 861–867 (2009).

<sup>21</sup> Lee, J. et al. Electrically tunable single- and few-layer MoS<sub>2</sub> nanoelectromechanical systems with broad dynamic range. Sci. Adv. 4, eaao6653 (2018).

<sup>22</sup> Frisenda, R. et al. Biaxial strain tuning of the optical properties of single-layer transition metal dichalcogenides. npj 2D Mater. Appl. 1, 10 (2017).

<sup>23</sup> Kim, H. H. *et al.* Magneto Memristive Switching in a 2D Layer Antiferromagnet. *Adv.* Mater. 32, 1905433 (2020).

<sup>24</sup> Kittel, C. Model of Exchange-Inversion Magnetization. *Phys. Rev.* **120**, 335–342

(1960). <sup>25</sup> Swoboda, T. J., Cloud, W. H., Bither, T. A., Sadler, M. S. & Jarrett, H. S. Evidence for an Antiferromagnetic-Ferrimagnetic Transition in Cr-Modified Mn2Sb. Phys. Rev. Lett. **4**, 509–511 (1960).

<sup>26</sup> Levitin, R. Z., and K. Ponomarev. Magnetostriction of the metamagnetic iron-rhodium alloy. Soviet Physics JETP 23.6 984-985. (1966).

<sup>27</sup> Hall, R. C. Single Crystal Anisotropy and Magnetostriction Constants of Several Ferromagnetic Materials Including Alloys of NiFe, SiFe, AlFe, CoNi, and CoFe. J. Appl. Phys. 30, 816–819 (1959).

<sup>28</sup> Šiškins. M. et al. Magnetic and electronic phase transitions probed by nanomechanical resonance, arXiv:1911.08537

<sup>29</sup> Storch, I. R. *et al.* Young's modulus and thermal expansion of tensioned graphene membranes. Phys. Rev. B 98, 085408 (2018).

<sup>30</sup> Shin, K.-H., Inoue, M. & Arai, K.-I. Strain sensitivity of highly magnetostrictive amorphous films for use in microstrain sensors. J. Appl. Phys. 85, 5465–5467 (1999).

# 370371 Data availability

The data that support the findings of this study are available within the paper and its Supplementary Information. Additional data are available from the corresponding authors upon request.

# 

# **Competing interests**

The authors declare no competing interests.

## 

## Acknowledgements

This work was primarily supported by the Air Force Office of Scientific Research under award FA9550-18-1-0480 (development of the experimental setup) and FA9550-19-1-0390 (optical characterizations). It was partially supported by the National Science Foundation under DMR-1807810 (modeling) and the Cornell Center for Materials Research with funding from the NSF MRSEC program under DMR-1719875 (sample and device fabrication). This work was performed in part at Cornell NanoScale Facility, an NNCI member supported by NSF Grant NNCI-1542081. K.F.M. acknowledges support from a David and Lucille Packard Fellowship.

# 

#### **Contributions**

S.J., K.F.M., J.S. and H.X. designed the study, discussed the results and co-wrote the manuscript. H.X. and S.J. developed the experimental setup and fabricated the devices. S.J. performed the bulk of the measurements and data analysis, assisted by H.X.

## 

## Figure captions

**Fig. 1: 2D** CrI<sub>3</sub> mechanical resonators. **a,** Schematic of the measurement system. The resonator (suspended 2D membrane on a Si trench of depth D) is actuated by an r.f. voltage from a vector network analyzer (VNA) through a bias tee. A DC voltage  $V_g$  is superimposed to apply static tension to the membrane. The motion is detected interferometrically by a HeNe laser, which is focused onto the center of the resonator. BS: beam splitter; PD: photodetector. **b,** Schematic of a bilayer CrI<sub>3</sub> resonator with

<sup>&</sup>lt;sup>31</sup> Lee, C., Wei, X., Kysar, J. W. & Hone, J. Measurement of the Elastic Properties and Intrinsic Strength of Monolayer Graphene. *Science* **321**, 385–388 (2008).

<sup>&</sup>lt;sup>32</sup> Liu, J., Sun, Q., Kawazoe, Y. & Jena, P. Exfoliating biocompatible ferromagnetic Crtrihalide monolayers. *Phys. Chem. Chem. Phys.* **18**, 8777–8784 (2016).

<sup>&</sup>lt;sup>33</sup> Zheng, F. *et al.* Tunable spin states in the two-dimensional magnet CrI3. *Nanoscale* **10**, 14298–14303 (2018).

<sup>&</sup>lt;sup>34</sup> Zhang, R., Koutsos, V. & Cheung, R. Elastic properties of suspended multilayer WSe2. *Appl. Phys. Lett.* **108**, 042104 (2016).

antiferromagnetic CrI<sub>3</sub> encapsulated by few-layer graphene and monolayer WSe<sub>2</sub>. Filled spheres and arrows denote Cr atoms and spins in the top and bottom CrI<sub>3</sub> layers. **c**, Optical microscope image of a bilayer CrI<sub>3</sub> device suspended over a circular trench. Dashed line shows the boundary of the CrI<sub>3</sub> flake. Scale bar is 4  $\mu$ m. **d**, Vibration amplitude (symbols) of bilayer CrI<sub>3</sub> resonator 1 (radius 2  $\mu$ m) vs. driving frequency and a Lorentzian fit of the resonance spectrum (solid line). **e**, Gate dependence of the measured resonance frequency (symbols) and fit to the continuum model (solid line) with initial stress  $\sigma_0 \approx 0.5 \ Nm^{-1}$ , mass density  $\rho \approx 3 \times 10^{-5} \ kgm^{-2}$  and effective Young's modulus  $Y_{eff} \approx 600 \ Nm^{-1}$ .

Fig. 2: Mechanical detection of the spin-flip transition in 2D CrI<sub>3</sub>. a, Normalized vibration amplitude of bilayer CrI<sub>3</sub> resonator 1 vs. driving frequency under an out-of-plane magnetic field  $(\mu_0 H_\perp)$  that sweeps from 1 T to -1 T to 1 T. b, Resonance frequency extracted from a as a function of magnetic field. c, Magnetic circular dichroism (MCD) of the membrane as a function of magnetic field. The red (blue) lines in b and c correspond to the measurement for the positive (negative) sweeping direction of the field. d-f, Same measurements as in a-c for 6-layer CrI<sub>3</sub> resonator 1 (radius 3  $\mu$ m).

**Fig. 3: Mechanical detection of spin canting in 2D CrI<sub>3</sub>. a**, Normalized vibration amplitude vs. driving frequency under an in-plane magnetic field  $(\mu_0 H_{||})$  that sweeps from 8 T to -8 T to 8 T for 6-layer CrI<sub>3</sub> resonator 1. **b**, Resonance frequency extracted from **a** as a function of magnetic field. Red (blue) symbols correspond to the measurement for the positive (negative) sweeping direction of the field. Dashed line is the expected quadratic dependence before saturation.

Fig. 4: Strain-tuning of the spin-flip transition in 2D CrI<sub>3</sub>. a, b, Normalized Magnetic circular dichroism (MCD) as a function of out-of-plane magnetic field ( $\mu_0 H_\perp$ ) that sweeps from - 1 T to 1 T (only - 0.6 T to 0.6 T is shown for clarity) at different gate voltages for a suspended (a) and a substrate-supported region (b) of bilayer CrI<sub>3</sub> resonator 1. c, Spin-flip transition field vs. gate voltage for the suspended (blue) and substrate-supported (red) region of the membrane. The lines are drawn to guide the eye. d, Spin-flip transition field as a function of gate-induced strain (symbols). The solid line is a linear fit.

# **Extended data figure captions**

**Extended Data Fig. 1: Mechanical resonance of 2D CrI<sub>3</sub> under an out-of-plane magnetic field. a, b,** Field dependence of the amplitude (a) and linewidth (b) of the fundamental resonance of bilayer CrI<sub>3</sub> resonator 1. The field dependence of the resonance frequency is shown in Fig. 2b. The red (blue) symbols correspond to the measurement for the positive (negative) field sweeping direction. c, Field dependence of the reflectance at 633 nm normalized by the reflectance at zero field.

- Extended Data Fig. 2: Summary of 6 CrI<sub>3</sub>-resonators under an out-of-plane 449 450 magnetic field. For each device, the contour plot shows the vibration amplitude vs. 451 driving frequency under an out-of-plane field that sweeps from the top to the bottom value. The other two panels compare the field dependence of the resonance frequency 452 (upper panel) and MCD (lower panel) of the membrane. The two colors denote the two 453 454 field sweeping directions. **a-c**, Bilayer CrI<sub>3</sub> resonator 1 (radius 2 μm), same as Fig. 2a-c. **d-f**, Bilayer CrI<sub>3</sub> resonator 2 (radius 2 μm). **g-i**, Trilayer CrI<sub>3</sub> resonator (radius 3 μm). **j-l**, 455 6-layer CrI<sub>3</sub> resonator 1 (radius 3 µm), same as Fig. 2d-f. m-o, 6-layer CrI<sub>3</sub> resonator 2 456 (radius 3 μm). p-r, 6-layer CrI<sub>3</sub> resonator 3 (radius 3 μm). MCD of the trilayer resonator 457 shows a ferromagnetic hysteresis loop centered at zero magnetic field (i), to which the 458 mechanical resonance is not sensitive (h). The insets in i show the spin configuration of 459 the system at given fields. 460
- Extended Data Fig. 3: Summary of 2 CrI<sub>3</sub>-resonators under an in-plane magnetic field. For each device, the contour plot shows the vibration amplitude vs. driving frequency under an in-plane field that sweeps from the top to the bottom value. The other panel is the field dependence of the resonance frequency. The two colors denote the two field sweeping directions. a,b, 6-layer CrI<sub>3</sub> resonator 1 (same as Fig. 3). c,d, 6-layer CrI<sub>3</sub> resonator 3.
- Extended Data Fig. 4: Inverse magnetostriction in 6-layer  $CrI_3$  resonator 2. a, Normalized MCD vs. out-of-plane magnetic field that sweeps from 2.2 T to -2.2 T (only 2 T to 0.5 T and -0.5 T to -2 T is shown for clarity) at different  $V_g$ 's. b, c, Strain dependence of the two spin-flip transition fields (symbols). The error bars correspond to the spin-flip transition widths. The solid lines are linear fits.
- Extended Data Fig. 5: Calibration of gate-induced strain and determination of 472 resonator parameters. a, Reflection contrast of bilayer CrI<sub>3</sub> resonator 1 from 1.6 – 1.9 473 eV as a function of gate voltage. The main feature is a dip (around 1.75 eV at  $V_a = 0 V$ ), 474 which corresponds to the fundamental exciton resonance of monolayer WSe2. The feature 475 redshifts slightly with  $V_q$  up to about 40 V followed by a larger redshift with further 476 increase of  $V_g$ . **b**, Representative spectra at selected  $V_g$ 's. **c**, Exciton resonance energy 477 extracted from a (left axis) and gate-induced strain calibrated from the exciton resonance 478 energy (right axis) as a function of  $V_a^4$  for  $V_a$  up to 39 V. The solid line is a linear fit. The 479 built-in stress  $\sigma_0$  was determined from the slope. 480
- Extended Data Fig. 6: 2D CrI<sub>3</sub> resonators under high out-of-plane fields. Normalized vibration amplitude vs. driving frequency under an out-of-plane magnetic field up to 5 T for 6-layer CrI<sub>3</sub> resonator 2. The resonance frequency, amplitude and linewidth basically do not change up to 5 T except at the spin-flip transitions.

485

486

Figure 1

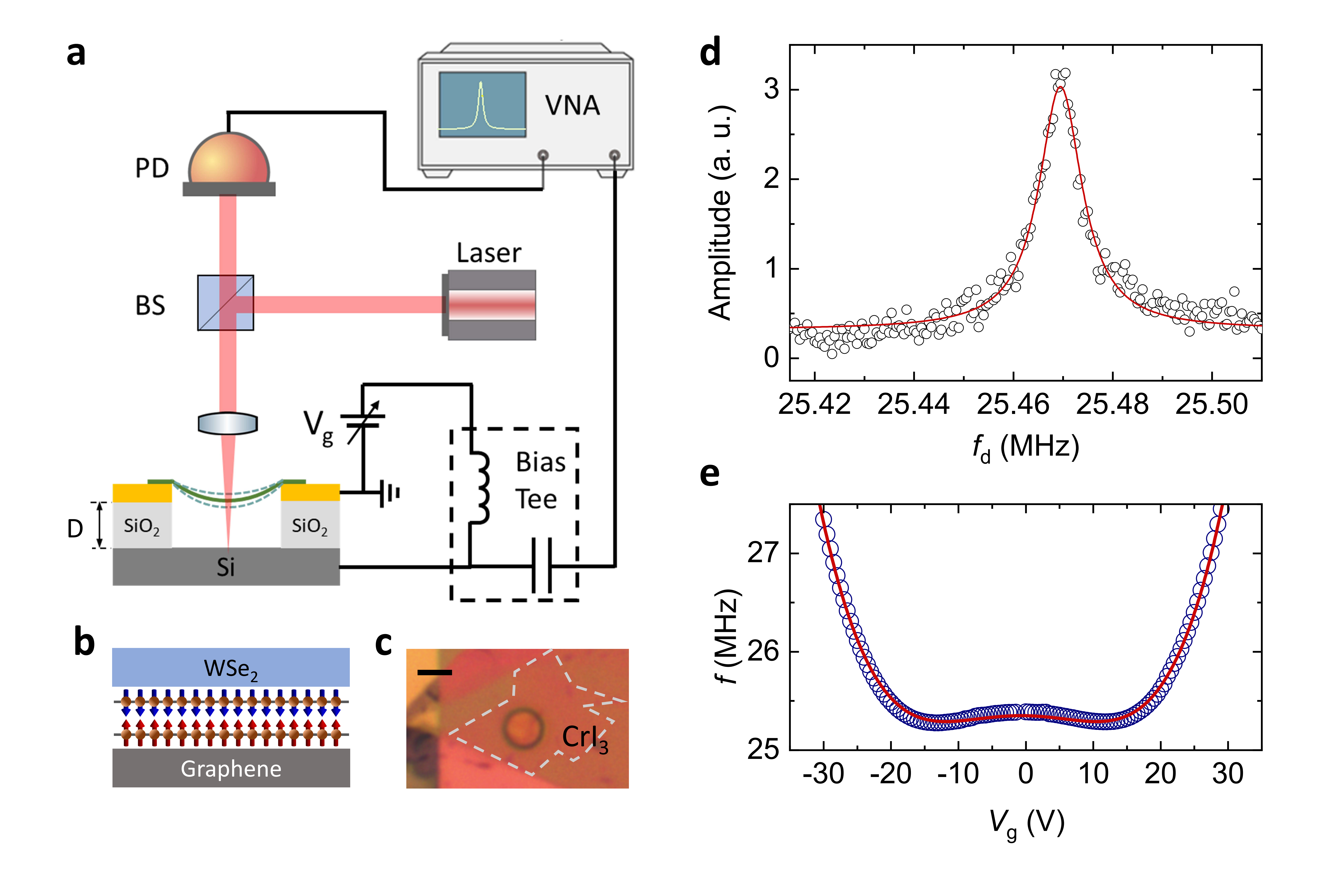


Figure 2

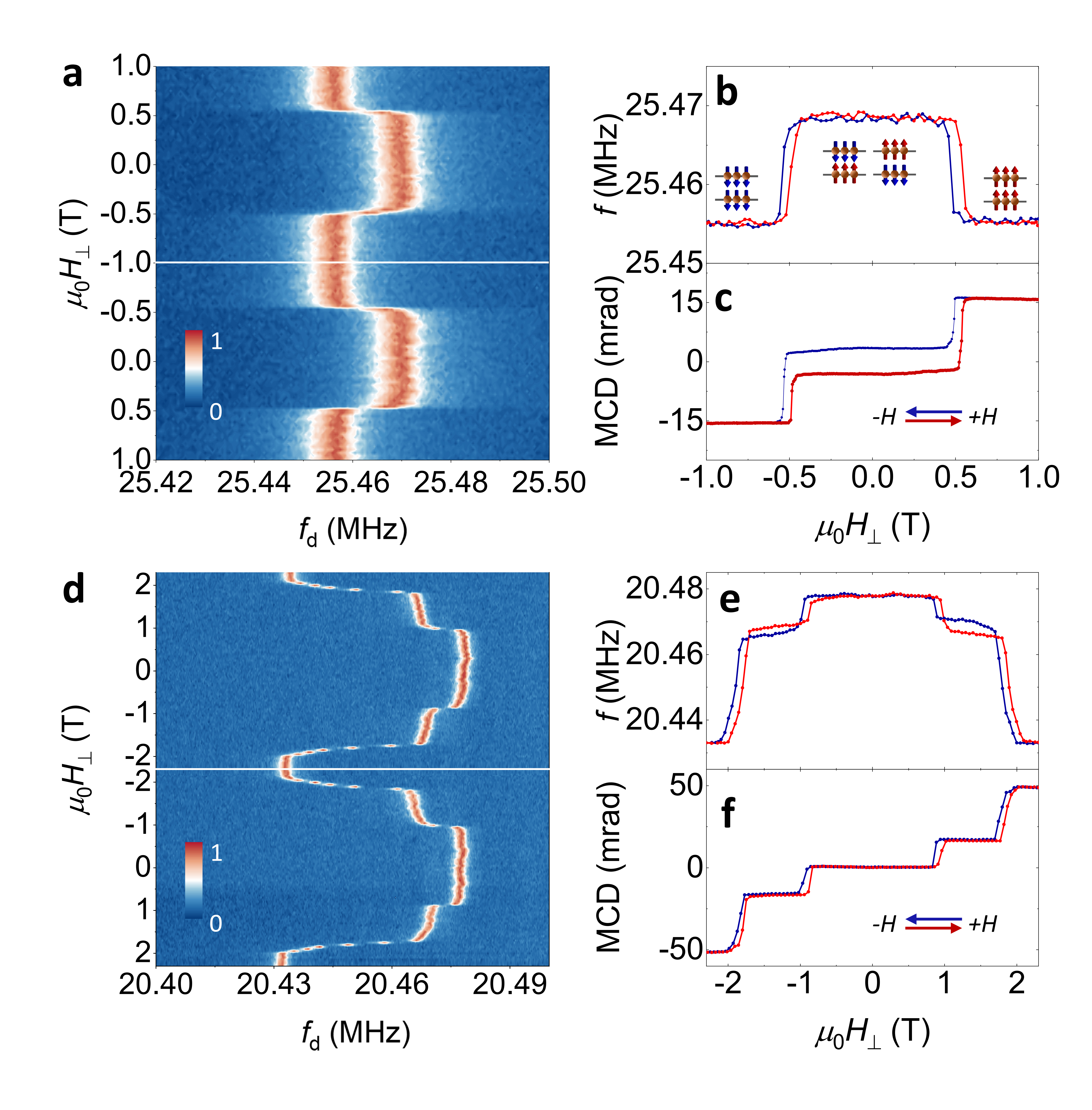


Figure 3

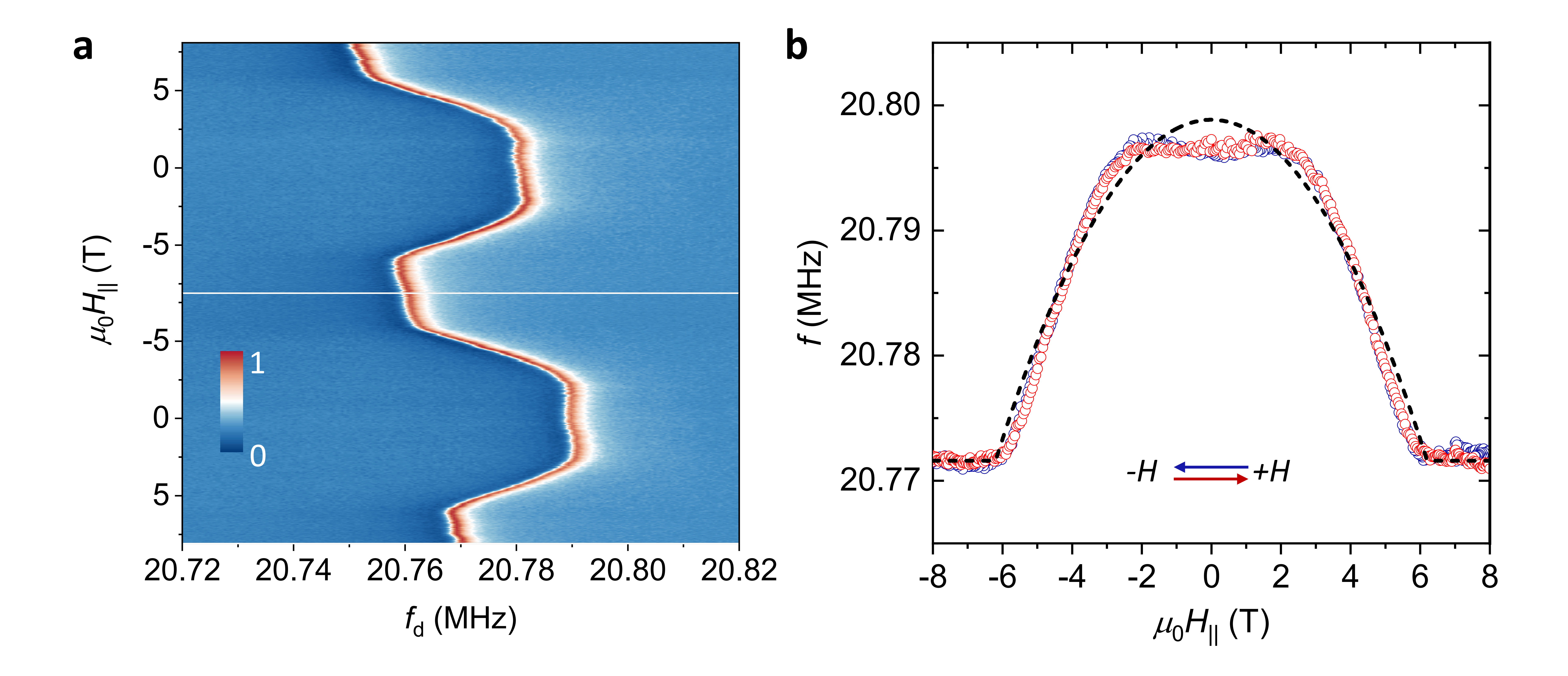


Figure 4

